Review

Analytical ABF-STEM imaging of Li ions in rechargeable batteries

Yuren Wen[1], Tongtong Shang[1], and Lin Gu[1,2,3,*]

[1]Beijing National Laboratory for Condensed Matter Physics, Institute of Physics, Chinese Academy of Sciences, Beijing 100190, China, [2]Collaborative Innovation Center of Quantum Matter, Beijing 100190, China, and [3]School of Physical Sciences, University of Chinese Academy of Sciences, Beijing 100190, China

*To whom correspondence should be addressed. E-mail: l.gu@iphy.ac.cn

Abstract

Rechargeable batteries are being intensively investigated in an attempt to solve the energy issues while meeting the environmental demands. Even though Li-ion batteries (LIB) with high energy and light weight have been commercialized within the last 20 years, these devices currently require higher energy density, output power and sustainability characteristics. The atomic behavior of Li ion that determines LIB's performance is hardly characterized by transmission electron microscopy (TEM) owing to its weak electron-scattering power. In this sense, annular bright-field (ABF) scanning TEM (STEM), in which the contrast has a low scaling rate with the atomic number, has been proven to be a robust technique for simultaneous imaging of light and heavy elements. The s-state model, in which electron channeling along the atomic column allows the intensity to be focusing in the forward direction, has successfully explained the theory of ABF contrast. Furthermore, the detector angle range, the defocus–thickness dependence and the accelerating voltage (among other parameters) were discussed for optimized imaging conditions. ABF-STEM has shown powerful capabilities in resolving the atomic structure and the chemistry of electrodes (e.g. Li-ion occupation and diffusion, phase transformation and interface reaction), thereby providing critical insights into the physical properties, the battery performance and the design guidance of LIB. The future directions of ABF imaging for the characterization of LIB materials were also reviewed.

Key words: scanning transmission electron microscopy, lithium-ion battery, annular bright-field, Li-ion diffusion

Introduction

With the aim to meet the ever-increasing energy demands of the growing global population and to overcome the pressing climate change and environmental protection challenges, renewable energy production and efficient energy storage with minimum emission or pollutant are hot topics worldwide. There are various renewable energy sources including wind, solar, tidal, biomass and geothermal. However, they are inherently intermittent and

generally dispersed as compared to the isolated, large-scale facilities that currently supply the vast majority of the electrical energy [1]. With the aim to make the best use of these energy sources, proper energy storage systems are needed. Rechargeable batteries combining high energy, light weight and low-cost characteristics are highly desirable and find numerous applications in a variety of fields (e.g. portable electronic, transportation and load-leveling, among others) [2].

The fast development of Li-ion batteries (LIB) has increased the demand for electrode materials having high-energy density, abundance, scalability and sustainability characteristics [3,4]. Thus, a deep understanding of the relationship between the microstructure and the battery performance as well as guidelines for designing better electrode materials are inevitably required [5]. Among various characterization tools, transmission electron microscopy (TEM) is a superior technique that provides information of localized structure and chemistry. In particular, the successful introduction of spherical aberration correctors [6,7], as originally suggested by Scherzer [8], has made it possible to reach sub-angstrom resolution [9–11].

Although the atomic behavior of Li ions often determines the electrochemical activity of LIB, these species are hardly detected by TEM owing to their weak electron-scattering power [12]. Yang *et al.* indirectly observed Li and oxygen from a $LiCoO_2$ cathode by experimental focal series of high-resolution TEM (HRTEM) images at 300 kV [13]. However, this method based on exit-surface wave reconstruction is not suitable for analyzing a wide range of cathode materials as it involves a series of complicated operation and simulation steps while having stringent specimen requirements [14].

With the aim to overcome the issues of HRTEM using a phase-contrast method, Pennycook *et al.* proposed a chemically sensitive high angle annular dark-field (HAADF) imaging technique for a scanning TEM (STEM) and obtained atomic number (Z) contrast [15]. STEM is a time-reversed form of TEM, as shown in Fig. 1 [16]. According to the principle of reciprocity in electron microscopy, the elastic-scattering amplitude from a source (Point A) to a detector (Point B) is equal to that from a source at B and detector at A. The direction of the rays is reversed from the TEM situation, with the elastic-scattering mechanism providing the same image contrast in both cases. However, when the specimen contains both heavy and light elements, the contrast derived from light elements (e.g. Li) may be overwhelmed by heavy elements during HAADF imaging as the image contrast is proportional to $Z^{1.7}$ [15,17].

By analogy with the hollow-cone illumination (HCI) technology in TEM, Okunishi *et al.* achieved direct visualization of light elements in 2009 by employing a novel

imaging mode for aberration-corrected STEM in which an annular detector was located within a bright-field momentum range [18]. As shown Fig. 2a, HCI employs selective rays within certain incident beam angle ranges instead of conventional axial illumination. HCI is known to
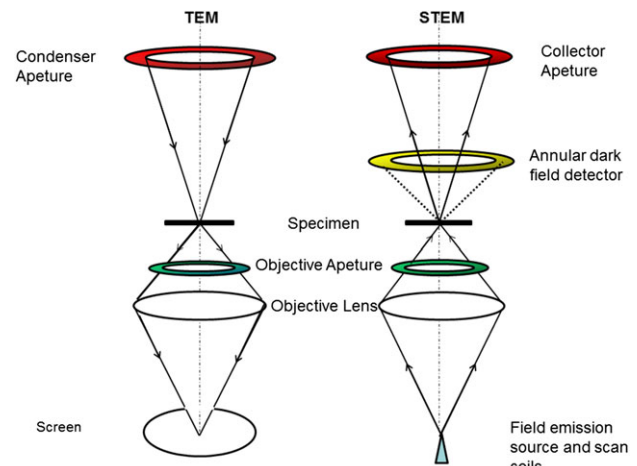

Fig. 1. Ray diagram of TEM and STEM showing the principle of reciprocity in electron microscopy. Reproduced with permission [16].
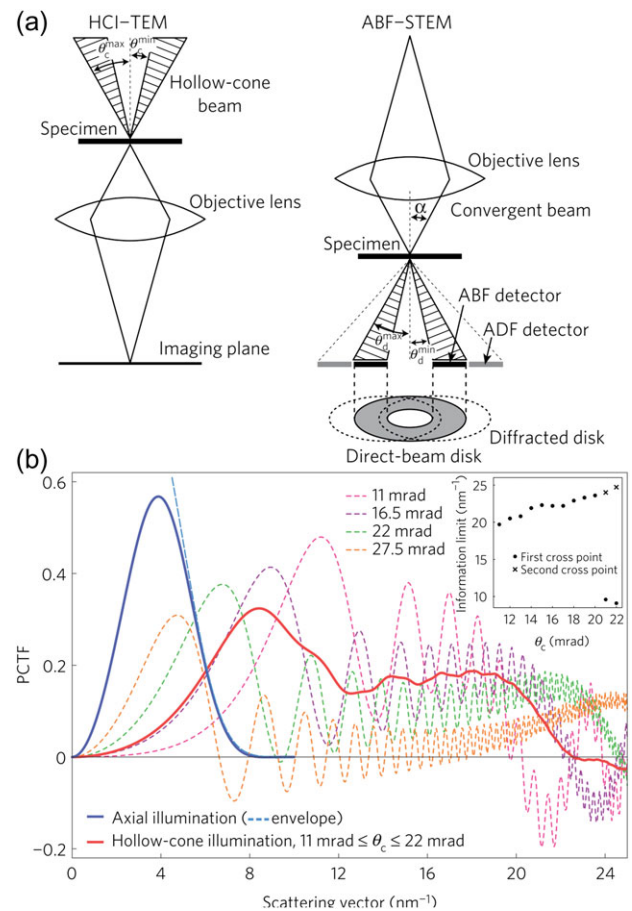

Fig. 2. (a) Ray diagram for HCI-TEM and ABF-STEM and (b) PCTF of HCI-TEM. Reproduced with permission [19].

significantly improve the resolution and the signal-to-noise ratio of a phase contrast by eliminating the chromatic aberration (C_c), which is the major factor limiting the resolution of HRTEM. Compared with axial illumination, HCI doubled the resolution at optimized conditions derived from the phase-contrast transfer function (PCTF). Similar to TEM and STEM, HCI-TEM can be reciprocally reversed by locating an annular detector within the bright-field region in STEM. The optimized hollow-cone condition (i.e. 11 mrad ≤ θ_c ≤ 22 mrad) derived from the aberration-corrected parameters shows that the information transfer can be extended to 22.5 nm^{-1} (Fig. 2b), which corresponds to a spatial resolution of ~44.4 pm [19]. This mode, termed as annular bright-field (ABF) imaging, is in accordance with the well-known HAADF imaging.

ABF imaging theory

Based on the HCI-TEM technology, the contrast transfer in reciprocal ABF imaging is expected to have better resolution than conventional bright-field STEM (BF-STEM), and, unlike BF-STEM, its non-oscillating nature provides easily interpretable images [18]. ABF imaging has received extensive attention after the first ABF imaging work, and plenty of experimental and theoretical evidences have further demonstrated that this technique allows reliable and simultaneous visualization of light and heavy elements over a range of specimen thicknesses [19–21]. With the aim to illustrate its advantages, the theory framework of ABF imaging will be presented with respect to its quantitative description and parameters optimization.

The s-state channeling model

With the aim to understand the contrast formation mechanism during ABF imaging, it is necessary to understand the electron-scattering phenomenon inside the specimen and its influence on the distribution of electrons reaching the detector plane. However, the scattering behavior of the electron probe inside the crystal can be very complex as it involves multiple elastic and inelastic scattering. While HAADF images are dominated by electrons undergoing thermal diffuse scattering (TDS), BF images tend to be dominated by coherent and elastic scattering. For simplicity, the effect of TDS is neglected as it represents a minor factor during ABF imaging of light elements [21]. Although the phase object approximation is a simple model that satisfactorily describes the elastic scattering, it has been shown unsatisfactory to explain ABF theory [21] and the s-state channeling model [22,23] was considered instead. By analogy with the 's-state' in the Bloch wave method, once the STEM probe locates well above the

atomic column, the total wave function can be divided into two contributions: (i) the s-state contribution which is highly localized around the atomic column; and (ii) the remainder contribution which could be included in the background term by using suitable simulations. When the incident electron probe is located above a column, the reciprocal space wave function can be expressed as a function of the propagation distance z inside the specimen as follows [24]:

$$\Psi_0(u, z) \approx \alpha\Phi_{1s}(u)\exp\left[-i\pi\frac{E_{00}}{E}\frac{z}{\lambda}\right] + [A(u) -\alpha\Phi_{1s}(u)]\exp[-i\pi\lambda u^2 z] \tag{1}$$

where Φ_{1s} is the s-state wave function, α is the s-state excitation amplitude, E_{00} is the s-state Eigen energy (negative), E is the accelerating energy, A is the reciprocal space probe-forming aperture function, λ is the electron wavelength and u is the two-dimensional reciprocal vector. Figure 3a shows the radial distribution of the diffraction pattern intensity as a function of the scattering angle β and the specimen thickness, as calculated from Eq. (1). Figure 3b shows the results calculated using the full multi-slice method. Although quantitative differences were found between both methods, the results were qualitatively well reproduced thereby validating the predictions of the s-state model. With the aim to define the detector range, Fig. 3c plots the wave functions of $\alpha\Phi_{1s}$, A and $A-\alpha\Phi_{1s}$ as a function of the scattering angle β as it appears in Eq. (1). The results can be roughly divided into three regions: (i) $0 \leq \beta \leq 10$ mrad, where $A-\alpha\Phi_{1s}$ is negative; (ii) $10 \leq \beta \leq 22$ mrad,
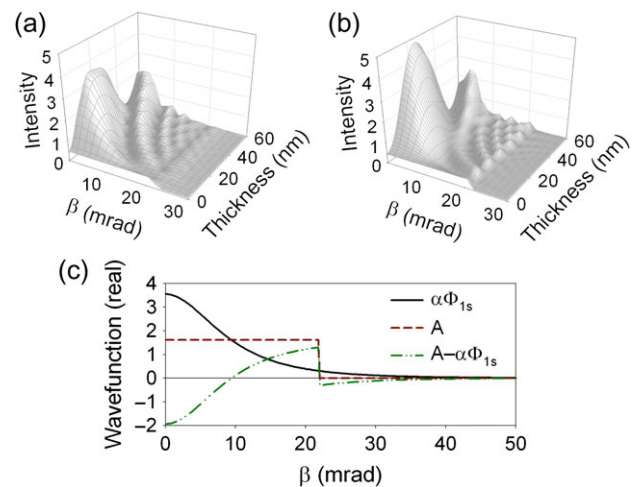
Fig. 3. Radial distribution of the diffraction pattern intensity as a function of the scattering angle and the sample thickness using (a) the s-state model and (b) full multi-slice simulation. (c) Plots of the quantities $\alpha\Phi_{1s}$, A and $A-\alpha\Phi_{1s}$ in Eq. (1) as a function of the scattering angle. A 200 kV, aberration-free STEM probe with a probe-forming semiangle of 22 mrad was positioned upon the O column in SrTiO3. Reproduced with permission [20].

where $A-\alpha\Phi_{1s}$ is positive and (iii) $\beta \geq 22$ mrad, where $A -\alpha\Phi_{1s}$ is negative again. In the first and third of the three regions, the two terms of $\alpha\Phi_{1s}$ and $A-\alpha\Phi_{1s}$ start perfectly out of phase (a phase shift of π) and their interference can only increase the total amplitude thereby resulting in a net increase of the electron density in these regions. However, the two terms start perfectly in phase (a phase shift of 0) in the middle region. When propagation changes the relative phase between these two terms, they inevitably go more out of phase. Thus, the interference can only reduce the total amplitude thereby resulting in a net reduction of the electron density in this region. This explains the deficit and absorptive image contrast of the ABF detector [20].

With the aim to summarize the above model into a simple picture, Fig. 4 shows the scattering from a light-, a heavy-element column, and the region between columns and their intensity locations on the ABF detector. When the probe is positioned right above the space between columns (Fig. 4a), the probe is largely unaffected by the interaction with the specimen thereby accounting for the background signal for reference. Figure 4b represents the probe positioned on the top of a light-element column. As the s-state model describes, channeling along this column consistently leads to a focus of the intensity in the forward direction which is blocked by the beam stopper in the ABF detector. Accordingly, the intensity reaching the ABF detector is reduced and the atomic column has a dark contrast appearance in the ABF imaging. Figure 4c shows the probe positioned atop a heavy-element column. A large portion of the probe is scattered to the high angle region thereby significantly reducing the signal reaching the ABF detector. Thus, the heavy-element atomic column appears even darker as compared to that of a light element. The absorption produced by TDS is the main cause accounting for the dark contrast of heavy elements in ABF imaging.
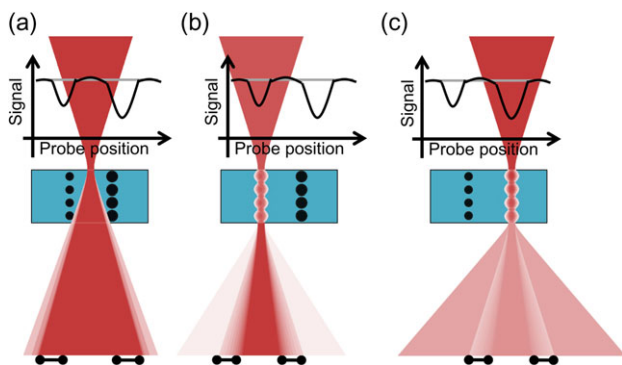
Fig. 4. Schematic of the electron probe scattering through an atomic column and onto an ABF detector (black dumbbells) with the probe positioned: (a) between the columns, (b) upon a light-element column and (c) upon a heavy-element column. Reproduced with permission [24].

Detector range

With the aim to simulate the distribution of electron intensity on the ABF detector plane, the diffraction imaging method (DI, Gatan Inc.) at atomic columns was performed on a $SrTiO_3$ sample orientated along the [001] zone axis. Figure 5a–c and e shows the high-resolution STEM images reconstructed from the 4D data cubes of the diffraction patterns. The Sr and Ti+O columns showed dark contrast (Fig. 5a), which corresponds to a BF-L image reconstructed from Area 1 shown in Fig. 5d. Conversely, these columns exhibited bright contrast in Fig. 5e corresponding to an HAADF image reconstructed from Area 3. The BF-S image (Fig. 5b) reconstructed from Area 4 showed bright spots at the O columns. The ABF image (Fig. 5c) reconstructed from Area 2 showed additional weaker dark spots at O columns apart from the Sr and Ti+O columns. Figure 5f shows the intensity line profiles of BF-L, BF-S and ABF images from the rectangle regions represented in Fig. 5a–c. At the oxygen position, dull peaks (BF-L), relative sharp peaks (BF-S) and valleys (ABF image) were observed. Thus, the intensity of ABF is a residue after the subtraction of the BF-S intensity from that of the BF-L image. The above results illustrated that the electron passing through a column of light elements converged to the central area of a direct beam disk, as explained by the s-state model [25].

Specifically, detailed simulations have revealed $\beta_{max} = \alpha$ (i.e. probe-forming aperture semiangle) as a good choice of outer detector angle. On the contrary, it appears that having $\beta_{min} = \beta_{max}/2$ is advantageous for balanced contrast and signal strength [21]. As a rough rule of thumb, the ABF contrast is approximately proportional to $Z^{1/3}$. However, this relation is not clear-cut and varies with the detector range and the probe-forming aperture semiangle, among other parameters [24].

Defocus–thickness dependence

Figure 6a–d shows the atomic resolved HAADF and ABF images for TiO_2 [001] and $SrTiO_3$ [110]. While the location of the O columns was not evident in the HAADF images, they were clearly visible in the ABF images exhibiting dark contrast. ABF images allowed for clearer visibility while enhancing the strength and contrast of light elements as compared to the corresponding HAADF images. Figure 6e shows a simulated defocus–thickness map for $SrTiO_3$ [110]. The ABF signal possessed an absorptive contrast as predicted by the s-state model. Thus, the simulated ABF images showed high contrast in the useful defocus range of ± 3 nm and over a wide range of sample thicknesses. Experimental studies on ABF imaging using aberration-corrected STEM further revealed atomic columns with dark contrast over a
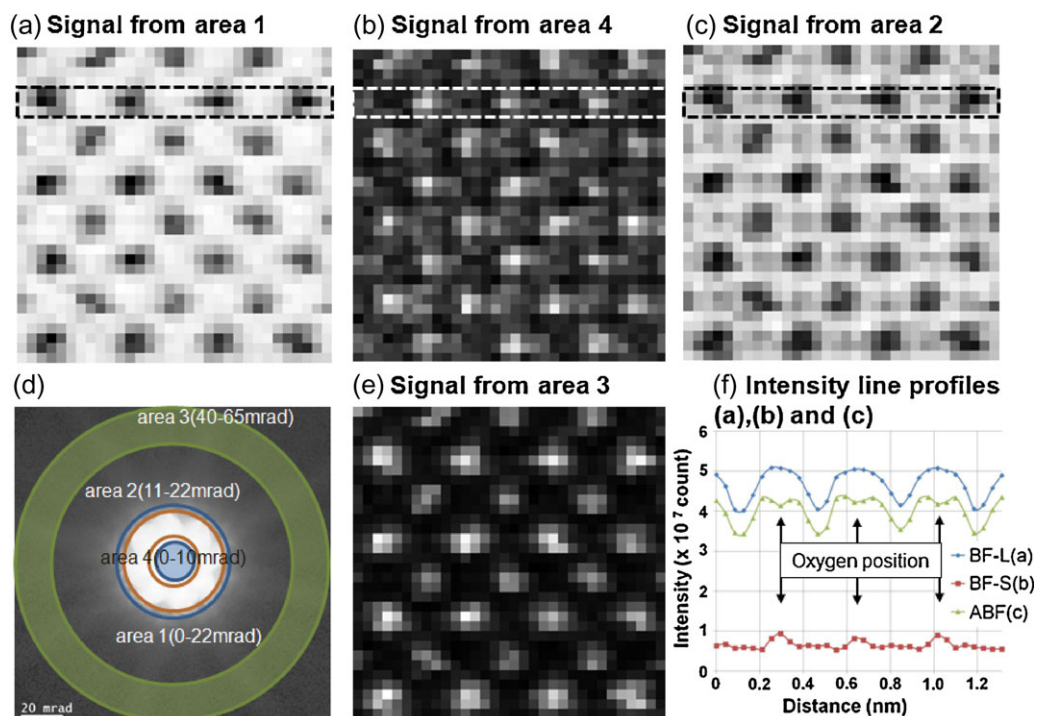
Fig. 5. HR-STEM images (a–c, e) and the corresponding intensity line profiles (f) reconstructed from the diffraction patterns of all scanned pixels stored in the four-dimensional data cube using signals from different areas of the diffraction plane as illustrated in (d). Reproduced with permission [25].
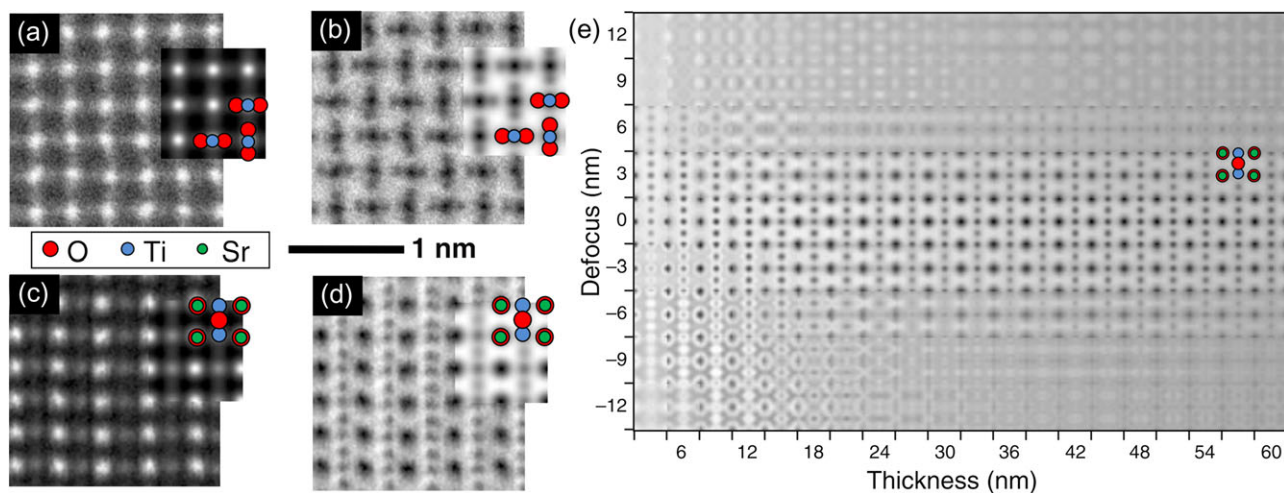
Fig. 6. HAADF and ABF images of (a) and (b) TiO2 [001], (c) and (d) SrTiO3 [110]. The simulated images and atomic structures are given in the insets. (e) Defocus–thickness map for the ABF imaging of SrTiO3 [110]. The microscope used was an aberration-corrected JEOL ARM200F operating at 200 kV with a probe-forming aperture semiangle of 22 mrad. Reproduced with permission [20].

wide range of thicknesses (10–70 nm) and defocus (–20 to +20 nm) [25].

The above results can also be applied to Li imaging. In this sense, higher accelerating voltage (e.g. 300 kV) is preferred for lithium contrast [26]. Further enhanced ABF imaging, generated upon subtraction of the middle-angle bright-field (0–9.4 mrad collection angle) from the ABF

signal, has shown enhanced detectability and contrast of light elements [27,28]. Moreover, it is noted that the ABF detector geometry is generally implemented using a BF detector and a beam stop. Although ABF-STEM cannot be acquired together with EELS, it could be simultaneously acquired with the atomic resolution EDX spectrum imaging [21].

Li insertion electrodes

Current commercial LIB uses electrode materials exhibiting an insertion redox reaction mechanism for both cathode and anode electrodes. While the chemistry of any electrode material determine the voltage range in which it is electrochemically reactive, the crystal structure of the electrode material often plays a critical role in determining the shape of the voltage profile as a function of the Li concentration. While the relationship between the voltage profile and the crystal structure of intercalation compounds is well known, the kinetic behavior of these materials (e.g. Li diffusion, phase transformation and interface reaction, among other parameters) is largely unknown because these processes are hardly distinguished by experimental work [29]. Since the pioneering works on ABF visualization of Li ions [30–34], ABF imaging has evolved into an powerful tool for analyzing the atomic structure and the chemistry of Li ions in cathode materials categorized by their Li transport behavior [35].

1D transport

Polyanionic compounds, containing large polyanions $(XO_4)^{y-}$ of earth abundant and environment-friendly elements (X = S, P, Si, As, Mo, W, among others), are being explored as alternative materials in replacement of transition metal (TM) oxides commonly used in modern portable devices. The $(XO_4)^{y-}$ framework, having strong X−O covalent bonds, increases the potential owing to the strong polarization of the oxygen ions toward the X cation [36]. One typical example of this class of compounds is olivine $LiFePO_4$. This material has received considerable attention as a positive electrode since the pioneer work from Padhi *et al.*, who demonstrated that Li ions can be extracted reversibly at a high voltage (~3.5 V vs Li^+/Li) via a two-phase mechanism involving Li-poor (Li_xFePO_4) and Li-rich ($Li_{1-x}FePO_4$) phases [37].

The good characteristics of $LiFePO_4$ as an electrode material has prompted many reports and debates on its physical properties including ionic and electronic conductivities, aliovalent cation doping, phase transition, size effect and surface coating [36]. The crystal structure of olivine $LiTMPO_4$ (TM = Fe, Ni, Mn or Co, among others) is shown in Fig. 7a [38]. Layers of octahedral TMO_6 (yellow) are corner shared in the *bc* plane, while linear chains of octahedral LiO_6 (green) are edge-shared along the *b* axis, thereby creating Li tunnels in this direction. It has been shown that Li-ion transport along the *b* axis is preferred [39,40]. Further modeling showed that the migration between adjacent Li sites in the [010] direction take place along a curved pathway in $LiFePO_4$ rather than by linear
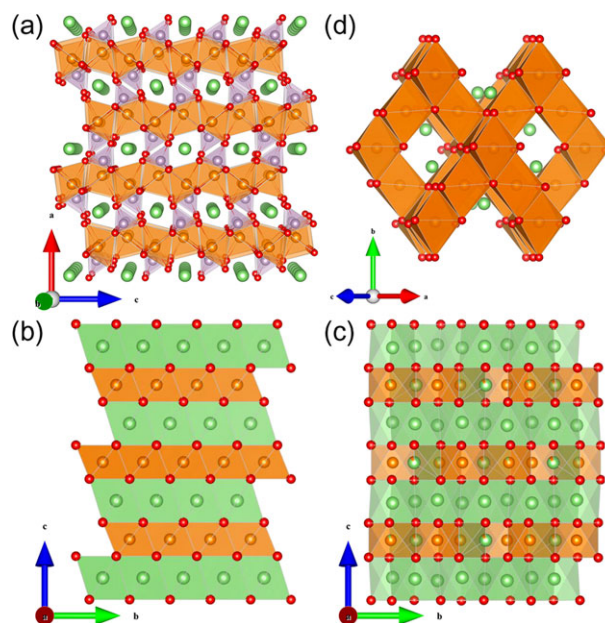

Fig. 7. Crystal structure of (a) olivine $LiTMPO_4$ illustrating the 1D Li-ion diffusion channels along the [010] direction, (b, c) layered cathode materials $LiTMO_2$ and Li_2MnO_3, (d) 3D spinel framework along the [101] direction. The Li atoms are in green, the O atoms are in red, the P atoms are in purple and the TM atoms in yellow. Structure visualization using the VESTA software [38].

hopping [41]. Diffusion of Li ions through a 1D channel can be impeded by immobile point defects such as antisite defects [42,43]. This brings out a unique phenomenon in which the diffusion constant depends on the particle size with the diffusion being slower in the bulk as compared to nanoparticles [44]. The benefit of nanosizing $LiFePO_4$ does not only arise from offering shortened transport paths but also from having enhanced diffusion constants. Thus, the characteristics of 1D Li-ion transport in $LiFePO_4$ are the key to understand its physical properties and the corresponding battery performances.

Intensive efforts were devoted to unravel the phase transition mechanism of $LiFePO_4$ as it exhibits ultrahigh discharge rates (even comparable to that of supercapacitors [45]) by optimized nanosizing and coating. Various two-phase mechanisms such as the domino-cascade model [46] have been proposed to explain the high-rate cycling capability of this material. Acquiring direct images at atomic resolution of partially delithiated $Li_{1-x}FePO_4$ is essential to clarify this question. Gu *et al.* [32] first observed Li staging in partially delithiated $LiFePO_4$ and found that the remaining Li ions preferably occupied every second layer. Such findings challenged the previously proposed two-phase separation mechanism.

Figure 8c shows an ABF image of partially delithiated $Li_{1-x}FePO_4$ ($x = $ ~0.5) acquired from the [010] direction. When compared with the pristine material (Fig. 8a, yellow
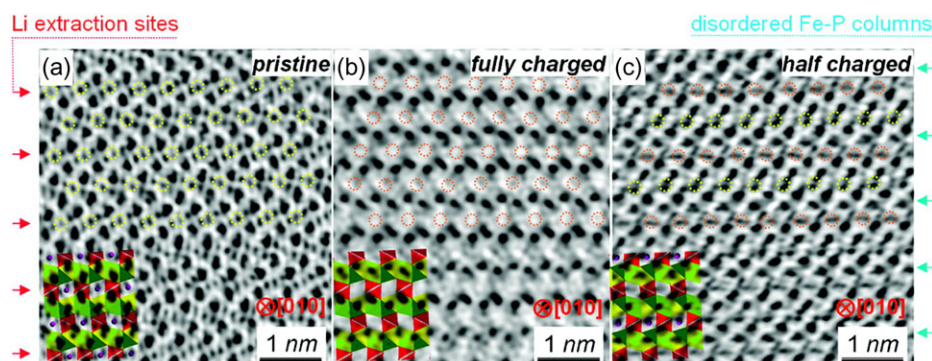
Fig. 8. ABF micrographs showing the Li ions location every row for partially delithiated LiFePO$_4$: (a) pristine state with the atomic structure of LiFePO$_4$, (b) fully charged state with the atomic structure of FePO$_4$ shown for comparison and (c) half charged state showing the Li staging structure. Li sites are marked by yellow circles while the delithiated sites are marked by orange circles. Reproduced with permission [32].

circles indicate Li ions), the Li ions in the delithiated material remained in the lattice occupying every other row (Fig. 8c). The Li extraction sites are indicated by red arrows. The crystal structures of LiFePO$_4$ and Li$_{0.5}$FePO$_4$ phases are shown in the insets of Fig. 8a and c, respectively. In the unit cell of Li$_{0.5}$FePO$_4$ (a fraction of Li ions is extracted) the upper nearby Fe−P columns (as indicated by cyan arrows) showed a fuzzy contrast, thereby indicating a local disordering of the structure. Consequently, a faint contrast corresponding to diffused O columns is observed close to the vacant sites in the rows where Li ions are extracted. The ABF image corresponding to fully charged FePO$_4$ (Fig. 8b) revealed that the distortion of the Fe−P columns disappeared with a more diffused distribution of O contrast around the pre-existed octahedral LiO$_6$.

Zhu *et al.* observed an ordered LiFePO$_4$–FePO$_4$ interface in partially delithiated LiFePO4 by ABF-STEM imaging. Figure 9a shows the ABF image of partially delithiated LiFePO$_4$ at the [010] zone axis. Three different phases appeared in Fig. 9a: (i) a pristine LiFePO$_4$ phase (cyan region, enlarged in Fig. 9b); (ii) FePO$_4$ phase (green region, enlarged in Fig. 9c); and (iii) an intermediate phase with a Li staging structure as shown in Fig. 8c (red region, enlarged in Fig. 9d). From the analysis of the ABF intensity profiles (the valleys of dark dots were inverted as peaks, Fig. 9e, f), the intensity of Li columns was significantly different in three regions. Thus, in the interface region (as separated by curved dashed lines), the intensity of the Li columns in Lines 1 and 3 was lower than that in Lines 2 and 4, thereby revealing a feature of Li staging structure. It is important to note that the interface frontier was a curved line and the occupancy of Li did not decrease from the LiFePO$_4$ to the FePO$_4$ region. It seems that the phase transition between LiFePO$_4$ and FePO$_4$ was propagated via an intermediate Li staging structure rather than by the two-

phase mechanism [47, 48]. The above direct observation of the interface structure strongly supported a solid-solution transformation mechanism of LiFePO$_4$ [49].

The phenomenon of Li staging in LiFePO$_4$ with different sizes (i.e. 70 and 50 nm) was also investigated. In larger crystals, the staging phase occurs at the interfacial zone (~15 nm width), whereas staging is found in smaller crystals throughout the matrix with a decrease of order from the center to the surface [48]. These findings further explain the benefit of nanosizing LiFePO$_4$ electrode materials in getting high-rate charging and discharging characteristics.

2D transport

Li ions in layered structures are generally thought to move via a 2D transport mechanism. There are many types of layered intercalation compounds such as graphite, TiNb$_2$O$_7$ [50], Li$_3$NbO$_4$ [51], LiCoO$_2$, LiNi$_{1/3}$Co$_{1/3}$Mn$_{1/3}$O$_2$, Ni-rich LiNi$_{0.8}$Co$_{0.15}$Al$_{0.05}$O$_2$ and Li- and Mn-rich electrode materials [4]. LiCoO$_2$ and its derivatives are widely used as cathode materials in mobile electronic devices. They have an ordered layered structure in which the Li and the TM slabs are alternately repeated in the cubic close-packed (ccp) frame of O atoms (Fig. 7b). Li and TM ions are positioned at the octahedral sites within the corresponding slabs. Most intercalation compounds undergo a variety of first-order phase transformations while changing the Li concentration. Thus, Li insertion into LiCoO$_2$ takes place with a change of the O stacking sequence from O3 (ABC) to O2 (ABAB) and O1 (AAA) types. The least energetically hindered hop path for Li diffusion between neighboring octahedral sites of a close-packed anion sublattice is along a curved path passing through an adjacent tetrahedral site via *o–t–o* diffusion. A Li-ion passing through a
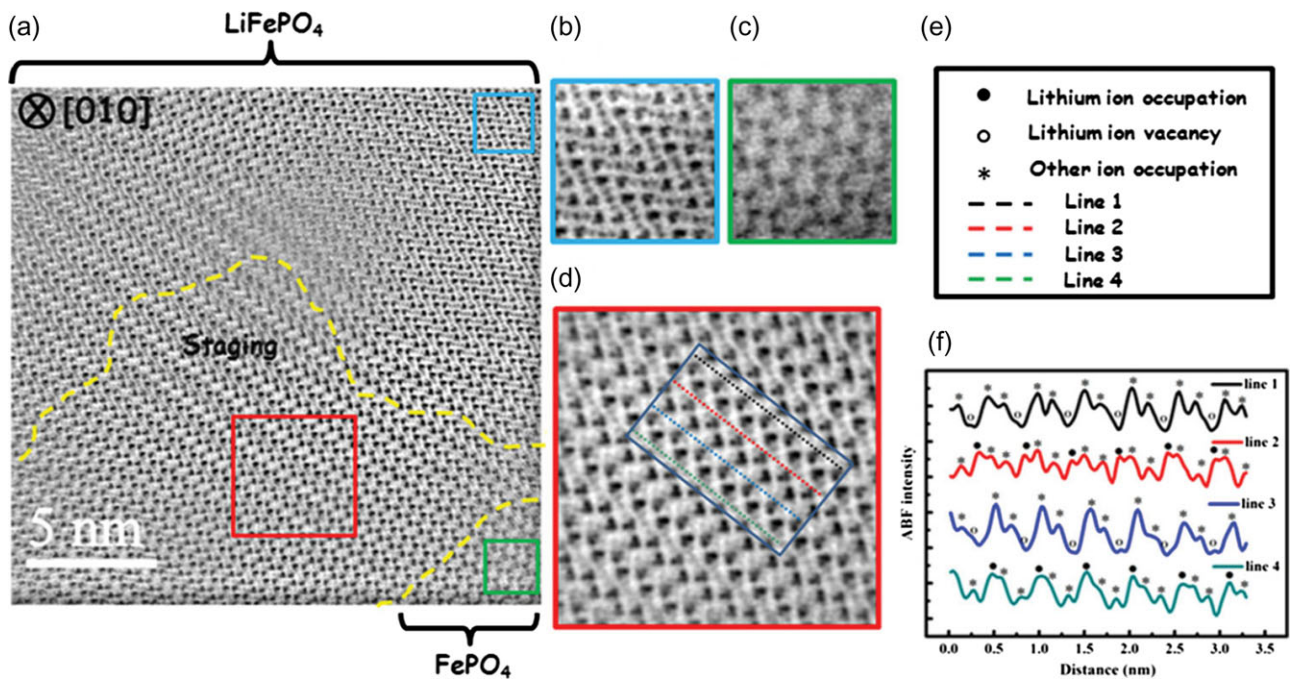
Fig. 9. (a) ABF images of a partially delithiated Nb-doped LiFePO₄ material along the [010] direction, and (b–d) magnified images and corresponding (e–g) atomic structures for different regions denoted by dashed rectangles. (h) Colored ABF intensity profiles from the corresponding dashed lines shown in (a). In the ABF line profiles, image contrast of dark dots was inverted and showed as peaks, same as below. Reproduced with permission [48].

tetrahedral site could also hop into a single vacancy or divacancy site. The energy of the intermediate tetrahedral site depends on its coordination extent by neighboring cations [29]. For example, the activated tetrahedral Li ion shares faces with four octahedral sites of Li, TM or vacancy sites. The energy of the intermediate state is largely determined by the electrostatic repulsion between the activated Li ion and its face-sharing species. Thus, the energy of the intermediate state depends on (i) the valence of the face-sharing species and (ii) the available space for relaxation between the activated Li ion and the face-sharing species. Cation-disordered structures have not been considered as cathodes because Li-ion diffusion tends to be blocked by its neighboring TM ions in Li slabs (i.e. 1-TM channel inactive). However, 0-TM channels become percolating above the Li content threshold in Li-excess cation-disordered materials [51,52]. Understanding 2D Li-ion transport may enable the design of both layered and Li-excess materials with high capacity and high-energy density characteristics.

The visualization of Li ions in LiCoO₂ using TEM was first reported elsewhere [13], and then clearly achieved by ABF-STEM [31]. The phase diagram during electrochemical cycling is complex and involves a variety of phases such as O3- and O2-types. The phase transitions are strongly related with the rearrangements of Li ions and Li

vacancies [53–55]. Lu *et al.* [56] employed STEM techniques to investigate the structural evolution of nanosized O3-Li₁₋ₓCoO₂ ($0 \leq x \leq 0.5$) cathodes including (i) arrangement of the Li ions and Li vacancies; (ii) distortion and (iii) phase transition. When the LiCoO₂ electrode was charged to 4.5 V (i.e. ~0.52 mol of Li extracted, Fig. 10b), O3-LiCoO₂ transformed into O1-LiCoO₂, as revealed by the Co columns arrangements. In Fig. 10b and c, the contrast of Co columns is alternately varied, which is significantly different from the black line obtained for the ABF micrograph of pristine LiCoO₂. The Co columns can be as Co1 and Co2, thereby indicating different chemical environments of Co ions in the Co-contained (003) plane after Li-ion extraction at high voltage. In Fig. 10d, the Li-ion columns (blue line) were also found to be different from the black line of pristine LiCoO₂. The Li-ion columns also showed a periodically varying contrast, in agreement with the simulated ABF image based on the Li ion and vacancy model (Fig. 10a). The O1-LiCoO₂ model shows that Li ions occupy every other (101) plane to form a staging structure.

Li₂MnO₃ is the parent compound of the next emerging cathode materials xLi₂MnO₃-(1−x)LiTMO₂ for high-energy density LIB. This Li-excess cathode material has a very high capacity for extracting more than 1 Li per formula. Compared with LiCoO₂, the TM plane of the
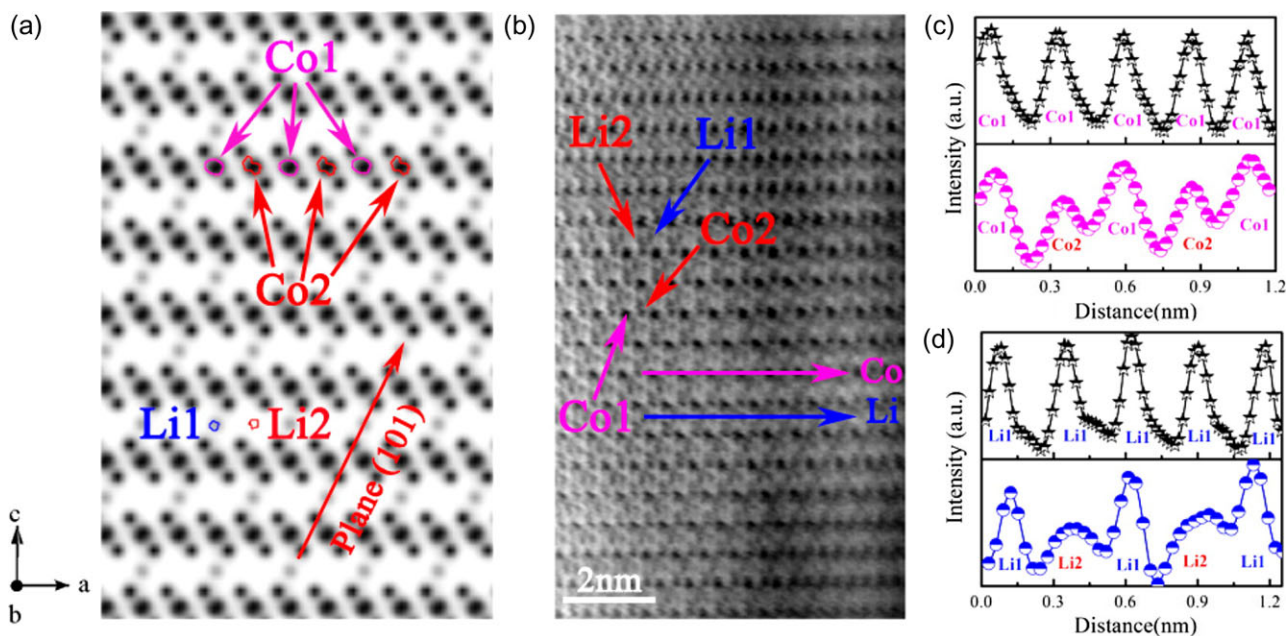
Fig. 10. (a) Simulated ABF micrographs of O1-type Li0.5CoO2 with ordered Li occupancies/vacancies arrangements at the [010] zone axis. (b) ABF-STEM image of a LiCoO2 electrode charged to 4.5 V at the [010] zone axis. The corresponding line profiles of (c) Co and (d) Li columns as arrowed in (b), where the black line was acquired from the ABF micrograph of pristine LiCoO2. Reproduced with permission [56].

Li-excess cathode contains additional Li columns. The Li_2MnO_3 structure can be written as $Li[Li_{0.33}Mn_{0.66}]O_2$ in which the $LiMn_2$ planes have an ordering within the cation arrangement (Fig. 7c). When viewed along the [110] zone axis, the $LiMn_2$ planes appear as a repeating sequence of 2 Mn and 1 Li columns, as shown in Fig. 11a. After delithiation, the line profiles of the $LiMn_2$ planes only showed the repeating sequence of 2 Mn columns (Lines 1 and 3 in Fig. 11b), thereby indicating that the Li ions at 2b site have been completely extracted. After discharge, the line profiles (Line 1 in Fig. 11c) revealed that the 2b site was again occupied by the reinserted Li. The Li planes consisted of Li atoms at the 2c and 4h sites in Li_2MnO_3. From Line 2 along the Li plane (Fig. 11a), the contrast of Li columns was nearly similar, thereby indicating uniform occupation of Li at these sites. After delithiation (Lines 2 and 4 in Fig. 11b), some gray spots marked by blue circles appeared just in the middle of the two consecutive Mn columns (i.e. above: Line 1, below: Line 3). These spots were at octahedral sites previously occupied by Li ions. Therefore, Mn should migrate into these sites after delithiation. After relithiation (Line 2 and Fig. 11c), it is interesting to note that the contrast along the Li plane was nearly similar, thereby indicating that the totality of Li was restored. This implies that the cation mixing of Mn into the Li planes seems reversible during the first cycles [57]. The above structural characterizations clearly reveal the Li extraction process and explain the high capacity obtained in Li_2MnO_3 and Li-excess cathode materials.

3D transport

Although Li ions can move within a ccp structure of layered oxides, these 2D Li diffusion materials have a degree of freedom along the *c* axis. The $LiTM_2O_4$ spinel structure (Fig. 7d), which also has a ccp frame of O atoms, presents fast Li transport in 3D. In the spinel oxide, the O anions occupying the 32e sites form a ccp framework, while TM cations reside in octahedral 16d sites and Li ions are located in tetrahedral 8a sites. After the first attempt to insert Li into the Fe_3O_4 spinel, it was described that Li ions pushed all Fe tetrahedral 8a sites into octahedral 16c sites leading to a phase transformation from ccp to a rock-salt phase [58]. Since then, other spinel structural oxides such as $LiMn_2O_4$ [59–61], $LiNi_yMn_{1-y}O_4$ [62,63] and $Li_4Ti_5O_{12}$ [64–66] have been widely investigated on their microstructure and properties relationship.

$LiMn_2O_4$ is a promising electrode material that has become an attractive alternative to layered $LiCoO_2$ owing to its high power capability, excellent safety, low-cost and environmental benign characteristics [60,67]. Nevertheless, it suffered from severe capacity fading, especially at the elevated temperatures associated with surface Mn^{2+} dissolution [68] in which Mn^{2+} is formed via disproportion $(2Mn^{3+} \rightarrow Mn^{2+} + Mn^{4+})$ under acidic conditions. In this sense, partial element substitution was effective in stabilizing $LiMn_2O_4$ since the shortage of one metal can be offset by the advance of another metal species. Thus, $Li(Ni_{0.5}Mn_{1.5})O_4$ has been extensively studied as a kind of high-voltage cathode materials [69–71].
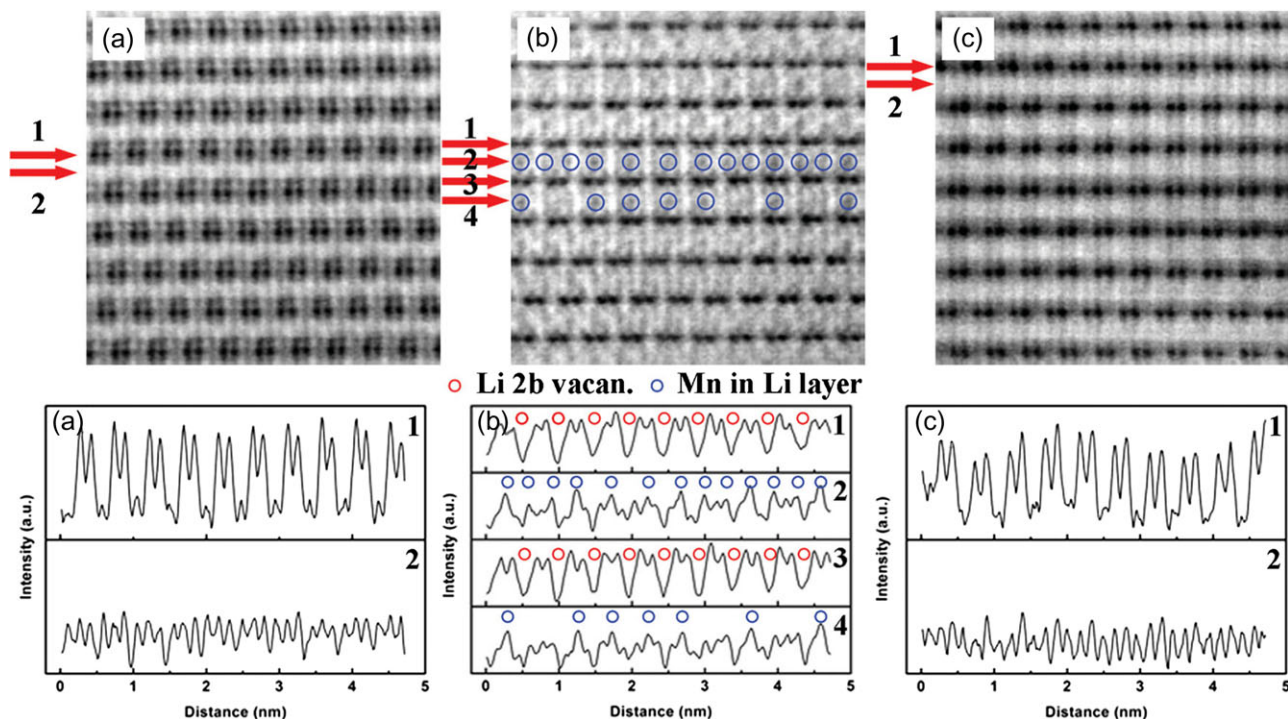
Fig. 11. ABF micrographs and the corresponding line profiles of Li ions in Li_2MnO_3 after the electrochemical lithiation and delithiation: (a) pristine Li_2MnO_3, (b) Li_2MnO_3 charged to 4.8 V and (c) Li_2MnO_3 discharged to 2 V after being charged to 4.8 V. Reproduced with permission [57].

$Li_4Ti_5O_{12}$, a spinel anode material, is the anode candidate with the greatest potential for being used in LIB owing to its intrinsic advantages [64,72]. Compared with commercial graphite (below 0.2 V vs Li/Li$^+$), $Li_4Ti_5O_{12}$ has a higher lithiation voltage plateau (1.55 V vs Li/Li$^+$) which can bring better safety of LIB while avoiding the formation of solid electrolyte interphase films [65,73]. Additionally, $Li_4Ti_5O_{12}$ exhibits excellent reversibility as a 'zero-strain' insertion material [74]. The structural formula of $Li_4Ti_5O_{12}$ can be described as $(Li)_{8a}[Li_{1/3}Ti_{5/3}]_{16d}(O_4)_{32e}$ during lithiation in which the Li ions at the 8a sites and inserted Li ions are cooperatively moved to the neighboring 16c sites to form the $(Li_2)_{16c}[Li_{1/3}Ti_{5/3}]_{16d}(O_4)_{32e}$ $(Li_7Ti_5O_{12})$ ordered rock-salt phase through a two-phase mechanism. Although the two-phase reaction mechanism for this $Li_4Ti_5O_{12}$ material has been well studied and clearly revealed [75,76], it is necessary to directly observe the phase transformation and the two-phase interface at atomic-scale. Lu *et al.* used ABF imaging to unambiguously reveal the Li storage mechanism in the $Li_4Ti_5O_{12}$ lattice at atomic-scale and to directly observe the two-phase interfacial structure for the first time [77]. As shown in Fig. 12, the phase boundary along the yellow curve revealed the coexistence of the two phases (i.e. $Li_4Ti_5O_{12}$ in Region 1 and $Li_7Ti_5O_{12}$ in Region 2), thereby verifying the two-phase reaction mechanism for the spinel $Li_4Ti_5O_{12}$. Comparing the profiles of the different regions in Fig. 12b and c, it can be clearly seen that Li is displaced from 8a to 16c sites, thereby demonstrating the Li diffusion

pathway in this spinel oxide. Figure 12d and e shows that the sharp coherent heterophase is consistent with the first-principles calculation and may be reasonably understood considering the 'zero-strain' characteristics of the lithiation/delithiation process of $Li_4Ti_5O_{12}$.

Perspectives

In summary, ABF-STEM has evolved into a powerful tool to visualize Li ions in rechargeable batteries. The weak electron scattering and contrast (overwhelmed by heavy elements) characteristics of Li atoms make this element difficult to be imaged by HRTEM or HAADF-STEM. Based on the s-state channeling mode, ABF imaging of light elements yields an absorption type of gray contrast as compared to the dark contrast of heavy elements. Under optimized conditions, it is possible to provide easily interpretable images with non-oscillating nature over a wide range of sample thicknesses and defocus. This promising imaging mode has shown robust capabilities in rechargeable batteries where the atomic behavior of Li ions is key to resolve their electrochemical properties. The electrode materials are divided into three categories according to their Li diffusion channel mechanism. ABF imaging has been revealed as a technique able to characterize the kinetic behavior (e.g. Li diffusion, phase transformation and interface reaction) of these intercalation compounds, which was previously difficult to be captured by experiments.
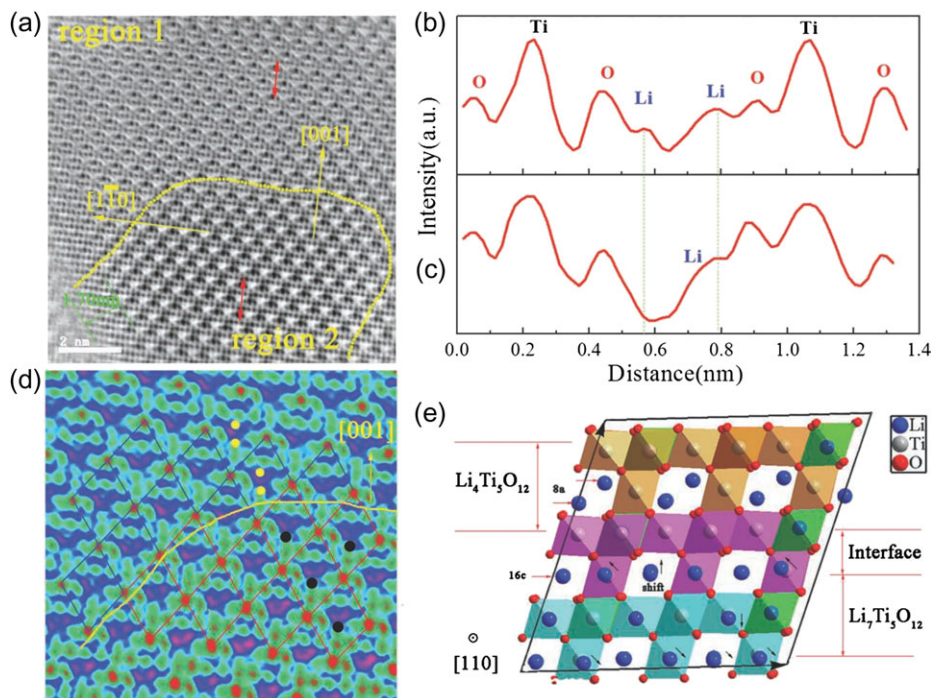
Fig. 12. Interfacial structure in a chemically lithiated $Li_4Ti_5O_{12}$ specimen along the [110] direction: (a) ABF image near the interface between the $Li_4Ti_5O_{12}$ phase (Region 1) and the $Li_7Ti_5O_{12}$ phase (Region 2). The yellow line indicates the boundary of the two-phase interface. (b, c) ABF line profile of Regions 1 and 2, respectively. (d) Colored ABF image of the two phases near the interface where the 8a sites occupied in $Li_4Ti_5O_{12}$ and the 16c sites occupied in $Li_7Ti_5O_{12}$ are marked as yellow and black dots, respectively. (e) Relaxed interfacial structure simulated by density functional theory where the Li16d-O octahedrons are shown in green. Reproduced with permission [77].

Solid-state batteries with high-energy density, high power and rigid safety advantages are under intensive investigation as near future storage devices [78]. The mechanism for ion diffusion in solid electrolytes is key to determine the kinetics of the electrochemical process [79]. Gao *et al.* [80] showed that ABF and EELS analyses can provide critical insights into the atomic structure and chemistry of solid ionic conductors. On the contrary, great efforts are needed to characterize the structure of the surface and the grain boundary as these interfaces contribute to the main resistance of ion conductivity [81–84]. Quantitative imaging of Li ions deserves further investigations to develop the ABF theory. Since the ABF contrast is nearly proportional to $Z^{1/3}$, the Li atoms in columns are countable and their intensity show a linear scaling with the number of unit cells [85]. Thus, it is promising to obtain atomic-scale information of the concentration of Li ions during battery operation.

References

1. Larcher D, Tarascon J M (2015) Towards greener and more sustainable batteries for electrical energy storage. *Nat. Chem.* 7: 19–29.
2. Whittingham M S (2008) Materials challenges facing electrical energy storage. *MRS Bull.* 33: 411–419.
3. Armand M, Tarascon J M (2008) Building better batteries. *Nature* 451: 652–657.
4. Choi J W, Aurbach D (2016) Promise and reality of post-lithium-ion batteries with high energy densities. *Nat. Rev. Mater.* 1: 16013.
5. Gu L, Xiao D, Hu Y-S, Li H, Ikuhara Y (2015) Atomic-scale structure evolution in a quasi-equilibrated electrochemical process of electrode materials for rechargeable batteries. *Adv. Mater.* 27: 2134–2149.
6. Haider M, Uhlemann S, Schwan E, Rose H, Kabius B, Urban K (1998) Electron microscopy image enhanced. *Nature* 392: 768–769.
7. Haider M, Rose H, Uhlemann S, Schwan E, Kabius B, Urban K (1998) A spherical-aberration-corrected 200 kV transmission electron microscope. *Ultramicroscopy* 75: 53–60.
8. Scherzer O (1949) The theoretical resolution limit of the electron microscope. *J. Appl. Phys.* 20: 20–29.

9. O'keefe M A, Hetherington C J D, Wang Y C, Nelson E C, Turner J H, Kisielowski C, Malm J O, Mueller R, Ringnalda J, Pan M, Thust A (2001) Sub-Ångstrom high-resolution transmission electron microscopy at 300 keV. *Ultramicroscopy* 89: 215–241.

10. Erni R, Rossell M D, Kisielowski C, Dahmen U (2009) Atomic-resolution imaging with a sub-50-pm electron probe. *Phys. Rev. Lett.* 102: 096101.

11. Tiemeijer P C, Bischoff M, Freitag B, Kisielowski C (2012) Using a monochromator to improve the resolution in TEM to below 0.5 Å. Part I: Creating highly coherent monochromated illumination. *Ultramicroscopy* 114: 72–81.

12. Senga R, Suenaga K (2015) Single-atom electron energy loss spectroscopy of light elements. *Nat. Commun.* 6: 7943.

13. Yang S-H, Croguennec L, Delmas C, Nelson E C, O'keefe M A (2003) Atomic resolution of lithium ions in $LiCoO_2$. *Nat. Mater.* 2: 464–467.

14. Rossell M D, Erni R, Asta M, Radmilovic V, Dahmen U (2009) Atomic-resolution imaging of lithium in Al_3Li precipitates. *Phys. Rev. B* 80: 024110.

15. Pennycook S J, Boatner L A (1988) Chemically sensitive structure-imaging with a scanning transmission electron microscope. *Nature* 336: 565–567.

16. Shang T-T, Liu X-Y, Gu L (2016) Interface of transition metal oxides at the atomic scale. *Sci. China Phys. Mech. Astron.* 59: 1–9.

17. Hillyard S, Silcox J (1995) Detector geometry, thermal diffuse scattering and strain effects in ADF STEM imaging. *Ultramicroscopy* 58: 6–17.

18. Okunishi E, Ishikawa I, Sawada H, Hosokawa F, Hori M, Kondo Y (2009) Visualization of light elements at ultrahigh resolution by STEM annular bright field microscopy. *Microsc Microanal.* 15: 164–165.

19. Ishikawa R, Okunishi E, Sawada H, Kondo Y, Hosokawa F, Abe E (2011) Direct imaging of hydrogen-atom columns in a crystal by annular bright-field electron microscopy. *Nat. Mater.* 10: 278–281.

20. Findlay S D, Shibata N, Sawada H, Okunishi E, Kondo Y, Yamamoto T, Ikuhara Y (2009) Robust atomic resolution imaging of light elements using scanning transmission electron microscopy. *Appl. Phys. Lett.* 95: 191913.

21. Findlay S D, Shibata N, Sawada H, Okunishi E, Kondo Y, Ikuhara Y (2010) Dynamics of annular bright field imaging in scanning transmission electron microscopy. *Ultramicroscopy* 110: 903–923.

22. Van Der Mast K D, Van Dyck D, Op De Beeck M (1996) A simple intuitive theory for electron diffraction. *Ultramicroscopy* 64: 99–107.

23. Geuens P, Dyck D V (2005) The S-state model for electron channeling in high-resolution electron microscopy. In: *Advances in Imaging and Electron Physics*, pp. 111–226 (Amsterdam: Elsevier).

24. Findlay S D, Shibata N, Ikuhara Y (2014) Theory for annular bright field STEM Imaging. In: *Scanning Transmission Electron Microscopy of Nanomaterials*, pp. 217–230 (London: IMPERIAL COLLEGE PRESS).

25. Okunishi E, Sawada H, Kondo Y (2012) Experimental study of annular bright field (ABF) imaging using aberration-corrected scanning transmission electron microscopy (STEM). *Micron* 43: 538–544.

26. Findlay S D, Lugg N R, Shibata N, Allen L J, Ikuhara Y (2011) Prospects for lithium imaging using annular bright field scanning transmission electron microscopy: A theoretical study. *Ultramicroscopy* 111: 1144–1154.

27. Ohtsuka M, Yamazaki T, Kotaka Y, Hashimoto I, Watanabe K (2012) Imaging of light and heavy atomic columns by spherical aberration corrected middle-angle bright-field STEM. *Ultramicroscopy* 120: 48–55.

28. Findlay S D, Kohno Y, Cardamone L A, Ikuhara Y, Shibata N (2014) Enhanced light element imaging in atomic resolution scanning transmission electron microscopy. *Ultramicroscopy* 136: 31–41.

29. Van Der Ven A, Bhattacharya J, Belak A A (2013) Understanding Li diffusion in Li-intercalation compounds. *Acc. Chem. Res.* 46: 1216–1225.

30. Oshima Y, Sawada H, Hosokawa F, Okunishi E, Kaneyama T, Kondo Y, Niitaka S, Takagi H, Tanishiro Y, Takayanagi K (2010) Direct imaging of lithium atoms in LiV_2O_4 by spherical aberration-corrected electron microscopy. *J. Electron. Microsc. (Tokyo)* 59: 457–461.

31. Huang R, Hitosugi T, Findlay S D, Fisher C A J, Ikuhara Y H, Moriwake H, Oki H, Ikuhara Y (2011) Real-time direct observation of Li in $LiCoO_2$ cathode material. *Appl. Phys. Lett.* 98: 051913.

32. Gu L, Zhu C, Li H, Yu Y, Li C, Tsukimoto S, Maier J, Ikuhara Y (2011) Direct observation of lithium staging in partially delithiated $LiFePO_4$ at atomic resolution. *J. Am. Chem. Soc.* 133: 4661–4663.

33. Ikuhara Y H R, Findlay S D, Mizoguchi T, Shibata N, Hirayama T, Yamamoto T, Oki H (2010) New approach to characterize ceramics by Cs-corrected STEM-three dimensional observation and light elements visualization. In: *AMTC Letters*, pp. 14–15 (Japan Fine Ceramics Center, Japan).

34. Huang R, Ikuhara Y H, Mizoguchi T, Findlay S D, Kuwabara A, Fisher C A J, Moriwake H, Oki H, Hirayama T, Ikuhara Y (2011) Oxygen-vacancy ordering at surfaces of lithium manganese(III,IV) oxide spinel nanoparticles. *Angew. Chem. Int. Ed.* 50: 3053–3057.

35. Huang R, Ikuhara Y (2012) STEM characterization for lithium-ion battery cathode materials. *Curr. Opin. Solid State Mater. Sci.* 16: 31–38.

36. Ellis B L, Lee K T, Nazar L F (2010) Positive electrode materials for Li-ion and Li-batteries. *Chem. Mater.* 22: 691–714.

37. Padhi A K, Nanjundaswamy K S, Goodenough J B (1997) Phospho-olivines as positive-electrode materials for rechargeable lithium batteries. *J. Electrochem. Soc.* 144: 1188–1194.

38. Momma K, Izumi F (2008) VESTA: a three-dimensional visualization system for electronic and structural analysis. *J. Appl. Crystallogr.* 41: 653–658.

39. Morgan D, Van Der Ven A, Ceder G (2004) Li conductivity in Li_xMPO_4 (M = Mn, Fe, Co, Ni) olivine materials. *Electrochem. Solid-State Lett.* 7: A30–A32.

40. Li J, Yao W, Martin S, Vaknin D (2008) Lithium ion conductivity in single crystal $LiFePO_4$. *Solid State Ionics* 179: 2016–2019.

41. Nishimura S-I, Kobayashi G, Ohoyama K, Kanno R, Yashima M, Yamada A (2008) Experimental visualization of lithium diffusion in Li_xFePO_4. *Nat. Mater.* 7: 707–711.

42. Chung S-Y, Choi S-Y, Yamamoto T, Ikuhara Y (2008) Atomic-scale visualization of antisite defects in LiFePO$_4$. *Phys. Rev. Lett.* 100: 125502.

43. Chung S-Y, Choi S-Y, Lee S, Ikuhara Y (2012) Distinct configurations of antisite defects in ordered metal phosphates: comparison between LiMnPO$_4$ and LiFePO$_4$. *Phys. Rev. Lett.* 108: 195501.

44. Malik R, Burch D, Bazant M, Ceder G (2010) Particle size dependence of the ionic diffusivity. *Nano. Lett.* 10: 4123–4127.

45. Kang B, Ceder G (2009) Battery materials for ultrafast charging and discharging. *Nature.* 458: 190–193.

46. Delmas C, Maccario M, Croguennec L, Le Cras F, Weill F (2008) Lithium deintercalation in LiFePO4 nanoparticles via a domino-cascade model. *Nat. Mater.* 7: 665–671.

47. Suo L, Han W, Lu X, Gu L, Hu Y-S, Li H, Chen D, Chen L, Tsukimoto S, Ikuhara Y (2012) Highly ordered staging structural interface between LiFePO$_4$ and FePO$_4$. *Phys. Chem. Chem. Phys.* 14: 5363–5367.

48. Zhu C, Gu L, Suo L, Popovic J, Li H, Ikuhara Y, Maier J (2014) Size-dependent staging and phase transition in LiFePO$_4$/FePO$_4$. *Adv. Funct. Mater.* 24: 312–318.

49. Liu H, Strobridge F C, Borkiewicz O J, Wiaderek K M, Chapman K W, Chupas P J, Grey C P (2014) Capturing metastable structures during high-rate cycling of LiFePO$_4$ nanoparticle electrodes. *Science* 344: 1252817.

50. Lu X, Jian Z, Fang Z, Gu L, Hu Y-S, Chen W, Wang Z, Chen L (2011) Atomic-scale investigation on lithium storage mechanism in TiNb$_2$O$_7$. *Energ. Environ. Sci.* 4: 2638–2644.

51. Yabuuchi N, Takeuchi M, Nakayama M, Shiiba H, Ogawa M, Nakayama K, Ohta T, Endo D, Ozaki T, Inamasu T, Sato K, Komaba S (2015) High-capacity electrode materials for rechargeable lithium batteries: Li$_3$NbO$_4$-based system with cation-disordered rocksalt structure. *Proc. Natl. Acad. Sci.* 112: 7650–7655.

52. Lee J, Urban A, Li X, Su D, Hautier G, Ceder G (2014) Unlocking the potential of cation-disordered oxides for rechargeable lithium batteries. *Science* 343: 519–522.

53. Yang S-H, Levasseur S, Weill F, Delmas C (2003) Probing lithium and vacancy ordering in O3 layered Li$_x$CoO$_2$ (x ≈ 0.5): An electron diffraction study. *J. Electrochem. Soc.* 150: A366–A373.

54. Wolverton C, Zunger A (1998) First-principles prediction of vacancy order-disorder and intercalation battery voltages in Li$_x$CoO$_2$. *Phys. Rev. Lett.* 81: 606–609.

55. Carlier D, Saadoune I, Ménétrier M, Delmas C (2002) Lithium electrochemical deintercalation from O2 LiCoO$_2$: Structure and physical properties. *J. Electrochem. Soc.* 149: A1310–A1320.

56. Lu X, Sun Y, Jian Z, He X, Gu L, Hu Y-S, Li H, Wang Z, Chen W, Duan X, Chen L, Maier J, Tsukimoto S, Ikuhara Y (2012) New insight into the atomic structure of electrochemically delithiated O3-Li$_{(1−x)}$CoO$_2$ (0 ≤ x ≤ 0.5) nanoparticles. *Nano. Lett.* 12: 6192–6197.

57. Wang R, He X, He L, Wang F, Xiao R, Gu L, Li H, Chen L (2013) Atomic structure of Li$_2$MnO$_3$ after partial delithiation and re-lithiation. *Adv. Energ. Mater.* 3: 1358–1367.

58. Thackeray M M, David W I F, Goodenough J B (1982) Structural characterization of the lithiated iron oxides Li$_x$Fe$_3$O$_4$ and Li$_x$Fe$_2$O$_3$ (0<x<2). *Mater. Res. Bull.* 17: 785–793.

59. Thackeray M M, David W I F, Bruce P G, Goodenough J B (1983) Lithium insertion into manganese spinels. *Mater. Res. Bull.* 18: 461–472.

60. Thackeray M M, Johnson P J, De Picciotto L A, Bruce P G, Goodenough J B (1984) Electrochemical extraction of lithium from LiMn$_2$O$_4$. *Mater. Res. Bull.* 19: 179–187.

61. Thackeray M M, Yang S-H, Kahaian A J, Kepler K D, Vaughey J T, Hackney S A (1998) Structural fatigue in spinel electrodes in high voltage (4V) Li/Li$_x$Mn$_2$O$_4$ cells. *Electrochem. Solid State Lett.* 1: 7–9.

62. Kunduraci M, Amatucci G G (2008) The effect of particle size and morphology on the rate capability of 4.7 V LiMn$_{1.5+δ}$Ni$_{0.5−δ}$O$_4$ spinel lithium-ion battery cathodes. *Electrochim. Acta* 53: 4193–4199.

63. Lin M X, Ben L B, Sun Y, Wang H, Yang Z Z, Gu L, Yu X Q, Yang X Q, Zhao H F, Yu R, Armand M, Huang X J (2015) Insight into the atomic structure of high-voltage spinel LiNi$_{0.5}$Mn$_{1.5}$O$_4$ cathode material in the first cycle. *Chem. Mater.* 27: 292–303.

64. Ferg E, Gummow R J, Dekock A, Thackeray M M (1994) Spinel anodes for lithium-ion batteries. *J. Electrochem. Soc.* 141: L147–L150.

65. Arico A S, Bruce P, Scrosati B, Tarascon J-M, Van Schalkwijk W (2005) Nanostructured materials for advanced energy conversion and storage devices. *Nat. Mater* 4: 366–377.

66. Lu X, Gu L, Hu Y-S, Chiu H-C, Li H, Demopoulos G P, Chen L (2015) New insight into the atomic-scale bulk and surface structure evolution of Li$_4$Ti$_5$O$_{12}$ anode. *J. Am. Chem. Soc.* 137: 1581–1586.

67. Amatucci G, Tarascon J M (2002) Optimization of insertion compounds such as LiMn$_2$O$_4$ for Li-ion batteries. *J. Electrochem. Soc.* 149: K31–K46.

68. Hunter J C (1981) Preparation of a new crystal form of manganese dioxide: λ-MnO$_2$. *J. Solid State Chem.* 39: 142–147.

69. Talyosef Y, Markovsky B, Salitra G, Aurbach D, Kim H J, Choi S (2005) The study of LiNi$_{0.5}$Mn$_{1.5}$O$_4$ 5-V cathodes for Li-ion batteries. *J. Power Sources* 146: 664–669.

70. Wakihara M (2005) Lithium manganese oxides with spinel structure and their cathode properties for lithium ion battery. *Electrochemistry* 73: 328–335.

71. Park S H, Oh S W, Kang S H, Belharouak I, Amine K, Sun Y K (2007) Comparative study of different crystallographic structure of LiNi$_{0.5}$Mn$_{1.5}$O$_{4−δ}$ cathodes with wide operation voltage (2.0–5.0 V). *Electrochim. Acta* 52: 7226–7230.

72. Borghols W J H, Wagemaker M, Lafont U, Kelder E M, Mulder F M (2009) Size effects in the Li$_{4+x}$Ti$_5$O$_{12}$ spinel. *J. Am. Chem. Soc.* 131: 17786–17792.

73. Zaghib K, Dontigny M, Guerfi A, Charest P, Rodrigues I, Mauger A, Julien C M (2011) Safe and fast-charging Li-ion battery with long shelf life for power applications. *J. Power Sources* 196: 3949–3954.

74. Zhu G-N, Wang Y-G, Xia Y-Y (2012) Ti-based compounds as anode materials for Li-ion batteries. *Energ. Environ. Sci.* 5: 6652–6667.

75. Scharner S, Weppner W, Schmid-Beurmann P (1999) Evidence of two-phase formation upon lithium insertion into the Li$_{1.33}$Ti$_{1.67}$O$_4$ spinel. *J. Electrochem. Soc.* 146: 857–861.

76. Takami N, Hoshina K, Inagaki H (2011) Lithium diffusion in $Li_{4/3}Ti_{5/3}O_4$ particles during insertion and extraction. *J. Electrochem. Soc.* 158: A725–A730.

77. Lu X, Zhao L, He X, Xiao R, Gu L, Hu Y-S, Li H, Wang Z, Duan X, Chen L, Maier J, Ikuhara Y (2012) Lithium storage in $Li_4Ti_5O_{12}$ spinel: The full static picture from electron microscopy. *Adv. Mater.* 24: 3233–3238.

78. Hu Y-S (2016) Batteries: Getting solid. *Nat. Energ.* 1: 16042.

79. Kato Y, Hori S, Saito T, Suzuki K, Hirayama M, Mitsui A, Yonemura M, Iba H, Kanno R (2016) High-power all-solid-state batteries using sulfide superionic conductors. *Nat. Energ.* 1: 16030.

80. Gao X, Fisher C a J, Kimura T, Ikuhara Y H, Moriwake H, Kuwabara A, Oki H, Tojigamori T, Huang R, Ikuhara Y (2013) Lithium atom and A-site vacancy distributions in lanthanum lithium titanate. *Chem. Mater.* 25: 1607–1614.

81. Ma C, Rangasamy E, Liang C, Sakamoto J, More K L, Chi M (2015) Excellent stability of a lithium-ion-conducting solid electrolyte upon reversible Li^+/H^+ exchange in aqueous solutions. *Angew. Chem. Int. Ed.* 54: 129–133.

82. Ma C, Chen K, Liang C, Nan C-W, Ishikawa R, More K, Chi M (2014) Atomic-scale origin of the large grain-boundary resistance in perovskite Li-ion-conducting solid electrolytes. *Energ. Environ. Sci.* 7: 1638–1642.

83. Balke N, Jesse S, Morozovska A N, Eliseev E, Chung D W, Kim, Y, Adamczyk, L, Garcia R E, Dudney N, Kalinin S V (2010) Nanoscale mapping of ion diffusion in a lithium-ion battery cathode. *Nat. Nanotech* 5: 749–754.

84. Wang Z, Santhanagopalan D, Zhang W, Wang F, Xin H L, He K, Li J, Dudney N, Meng Y S (2016) In situ STEM-EELS observation of nanoscale interfacial phenomena in all-solid-state batteries. *Nano Lett.* 16: 3760–3767.

85. Lee S, Oshima Y, Sawada H, Hosokawa F, Okunishi E, Kaneyama T, Kondo Y, Niitaka S, Takagi H, Tanishiro Y, Takayanagi K (2011) Counting lithium ions in the diffusion channel of an LiV_2O_4 crystal. *J. Appl. Phys.* 109: 113530.